

Developing Iran's empirical zenith wet delay model (IR-ZWD)

Dehviri, Masood; Farzaneh, Saeed; Forootan, Ehsan

Published in:
Journal of Atmospheric and Solar-Terrestrial Physics

DOI (link to publication from Publisher):
[10.1016/j.jastp.2023.106163](https://doi.org/10.1016/j.jastp.2023.106163)

Publication date:
2023

Document Version
Early version, also known as pre-print

[Link to publication from Aalborg University](#)

Citation for published version (APA):
Dehviri, M., Farzaneh, S., & Forootan, E. (2023). Developing Iran's empirical zenith wet delay model (IR-ZWD). *Journal of Atmospheric and Solar-Terrestrial Physics*, 253, Article 106163.
<https://doi.org/10.1016/j.jastp.2023.106163>

General rights

Copyright and moral rights for the publications made accessible in the public portal are retained by the authors and/or other copyright owners and it is a condition of accessing publications that users recognise and abide by the legal requirements associated with these rights.

- Users may download and print one copy of any publication from the public portal for the purpose of private study or research.
- You may not further distribute the material or use it for any profit-making activity or commercial gain
- You may freely distribute the URL identifying the publication in the public portal -

Take down policy

If you believe that this document breaches copyright please contact us at vbn@aub.aau.dk providing details, and we will remove access to the work immediately and investigate your claim.

1 **Developing Iran’s empirical Zenith Wet Delay model (IR-ZWD)**

2 Masoud Dehvari¹, Saeed Farzaneh^{1,*}, Ehsan Forootan²,

3 ¹School of Surveying and Geospatial Engineering, College of Engineering, University of Tehran,
4 Tehran, Iran

5 ²Geodesy Group, Department of Planning, Aalborg University, Rendburggade 14, 9000 Aalborg,
6 Denmark.

7 *Corresponding author: Associate Professor, School of Surveying and Geospatial Engineering,
8 College of Engineering, University of Tehran, Tehran, Iran; * Farzaneh@ut.ac.ir

9 **Abstract**

10 The presence of water vapor in the lower atmosphere can introduce errors in satellite-based
11 geodetic observations. Accurate modeling of this part of atmospheric delay is particularly
12 challenging due to the considerable variations of water vapor. Therefore, constructing a reasonable
13 model to predict Zenith Wet Delay (ZWD) can improve the accuracy of geodetic observations and
14 positioning techniques. In this study, we aim at constructing a regional ZWD model for Iran and
15 nearby regions (called the IR-ZWD model) using base functions with local support. The mode is
16 based on the five-year outputs of the Empirical Reanalysis Fifth generation (ERA5) data with the
17 spatial resolution of about 0.25 degree from 2017-2021. The B-spline base functions are used to
18 effectively represent local spatial changes in the spectral domain and to decrease the number of
19 unknown parameters. A B-spline model with the order and surface resolution of about 3 and 5
20 (scalar values) is found to be efficient, which has an equivalent spatial resolution of ~0.5 degree.
21 Temporal variations are accounted for by applying a constant term, along with periodic
22 components with annual, semi-annual, 3-, and 4-monthly periods. Our results demonstrate that the
23 proposed model has a mean Root Mean Squared Error (RMSE) of about 0.035 m within Iran,
24 which represents an improvement of approximately 12.5% compared to the commonly used global
25 empirical models such as GPT3w, GTrop, and HGPT2. The squared correlation coefficient value
26 of 0.55 is found between IR-ZWD and ERA5 data, which is about 10% higher than that of, e.g.,
27 GPT3w and GTrop. The IR-ZWD model is also evaluated against five radiosonde stations and
28 ZWD from the Jason-3 satellite mission. In both cases, the results indicate that IR-ZWD can reduce
29 the RMSE and MAE values of about 10%, and it improves the squared correlation coefficient
30 value about 9%.

Commented [EF1]: Why squared?

Commented [EF2]: Why squared?

31 **Keywords:** Empirical model; Zenith Wet Delay (ZWD); ERA5; B-spline; radiosonde station;
32 Jason-3 mission

34 **1. Introduction**

35 Satellite geodetic observations of the Global Navigation Satellite System (GNSS) have been
36 frequently used for positioning, navigation, and remote sensing of atmospheric parameters (Bender
37 et al., 2011; Bevis et al., 1992; Forootan et al., 2021). GNSS observations are of very high temporal
38 resolution with the benefits of all-weather capabilities, and they induce relatively low cost (Sun et

39 al., 2017b). However, these observations encounter errors caused by the movement of GNSS signal
40 through the atmosphere, namely the ionospheric and tropospheric errors. The ionosphere delay can
41 be mitigated via dual frequency observations in the form of ionosphere-free or other types of
42 combinations (Subirana et al., 2013). Therefore, the remaining tropospheric delay, also known as
43 the Zenith Total Delay (ZTD), is a considerable error source, which cannot be reduced by
44 combining GNSS bands (Sun et al., 2017a). The ZTD consists of two parts, i.e., the Zenith
45 Hydrostatic Delay (ZHD) and the Zenith Wet Delay (ZWD), where ZHD can be modeled quite
46 precisely using surface pressure and temperature observations (Davis et al., 1985; Dogan and
47 Erdogan, 2022). The spatial and temporal variations of the ZWD are, however, driven by weather
48 and might contain many local features that make it difficult to be accurately modeled (Forootan et
49 al., 2021; Tunali and Özlüdemir, 2019). Presenting ZWD with high accuracy can be helpful for
50 predicting seasonal weather, and increasing the accuracy of space-based geodetic observations,
51 especially enhancing the accuracy of the Single Point Positioning (SPP) technique (Kalita and
52 Rzepecka, 2017; Tregoning and Herring, 2006; Vedel and Huang, 2004; Yan et al., 2009).
53 Therefore, it is beneficial to construct models that present ZWD as precisely as possible .

54 Many empirical models have been constructed to mitigate the effects of tropospheric delay, which
55 can be separated into two different types based on the required parameters. The first one consists
56 of empirical models such as the Hopfield model (Hopfield, 1969), the Saastamoinen model
57 (Saastamoinen, 1972), and the Black model (Black, 1978), which requires surface meteorological
58 parameters for the calculation of atmospheric delays. However, due to a lack of measurements
59 about the vertical profile of water vapor, the reliability of these models is found to be low (Yao
60 and Hu, 2018). Also, the real-time application of these models in positioning and navigation may
61 be limited due to the high dependence of models on meteorological measurements (Sun et al.,
62 2017b). The second category comprises empirical models that are constructed based on numerical
63 analysis or reanalysis datasets such as ERA5 (Hersbach et al., 2020), ERA-Interim (Dee et al.,
64 2011), or the Global Geodetic Observing System (GGOS) (Plag et al., 2009). From these models,
65 the UNB series (Collins and Langley, 1997), EGNOS (Penna et al., 2001), IGGtrop (Li et al.,
66 2012), GZTD Series (YAO et al., 2013; Yao et al., 2016), GZTDS (Sun et al., 2017a), GPT2w
67 (Böhm et al., 2015), IGPT2W (Du et al., 2020), GPT3w (Landskron and Böhm, 2018), GEOFT
68 (Sun et al., 2017b), GTrop (Sun et al., 2019), EGtrop (Ma et al., 2021), AGtrop (Ma et al., 2022),
69 and the HGPT series (Mateus et al., 2020; Mateus et al., 2021) have been constructed with global
70 coverage but with different spatial and temporal resolutions. The data source for the construction
71 of the mentioned models and the corresponding spatial resolution of each model are listed in Table
72 1.

73

74

Table 1. An overview of the available empirical atmospheric delay models.

Model	Spatial resolution(deg)	Source
UNB3	15	Multi source observations
EGNOS	15	European Centre for Medium-Range Weather Forecast (ECMWF) reanalysis dataset
IGGtrop	2.5	National Centers for Environmental Prediction (NCEP) reanalysis data
GZTD	18	GGOS ZTD data

GZTD2	10	GGOS ZTD data
GZTDS	2×2.5	GGOS ZTD data
GPT2w	1	ERA-Interim
IGPT2W	1	ERA-Interim
GPT3w	1	ERA-Interim
GEOFT	2.5	GGOS
GTrop	1	ERA-Interim
EGtrop	12	ERA5
AGtrop	1	ERA5
HGPT2	0.25	ERA5

75
76 The empirical models in Table 1 present the global average of tropospheric delay at the best spatial
77 resolution of about 1° (except HGPT2 model). Considering the high spatial changes of water vapor,
78 it can be concluded that these models have limitations for representing the regional spatio-temporal
79 changes of ZWD values. Also, these models calculate atmospheric delay in a grid-based approach
80 or using a functional model (e.g., in terms of spherical harmonics coefficients) with global support.
81 Compared with grid-based models, functional models might be more numerically stable, because
82 a smaller number of parameters needs to be computed to numerical build the model. For example,
83 for 1-degree resolution global ZWD model one needs to estimate 64800 parameters in the grid
84 domain, which is equivalent with 32761 coefficients in terms of spherical harmonics up to degree
85 and order 180. Among the empirical models listed in Table 1, the HGPT2 model is a grid-based
86 model for atmospheric parameters, featuring a spatial resolution of approximately 0.25 degrees.
87 This model is Constructed using 20 years of ERA5 data and incorporating a time segmentation
88 concept, which boasts an hourly temporal resolution.

89 The aim of this study is to produce an empirical ZWD model for Iran and nearby regions, which
90 is called here IR-ZWD. This model is constructed based on five years of the high-resolution ERA5
91 dataset from January 1, 2017 to 31 December 2021. IR-ZWD considers a constant component
92 along with the annual, semi-annual, 3-, and 4-monthly harmonics to account for the temporal
93 variations of the ZWD values. To represent the spatial anomaly maps, the B-spline base functions
94 (Limberger, 2015) are used. Compared with the functional model with global coverage (e.g.
95 spherical harmonics in (Dehvari et al., 2023; YAO et al., 2013; Yao et al., 2016), the B-splines can
96 retrieve the local features of ZWD with a lower number of required unknown coefficients.
97 Therefore, our motivation for selecting this configuration is the usage of a high-resolution dataset
98 (ERA5) for the reconstruction of the empirical ZWD model using base functions with local support
99 that benefits from a lower number of unknown parameters compared to the grid-based model. The
100 proposed model provides ZWD values with spatial resolution of about 0.5 degrees (B-spline
101 functions with order 3 and surface resolution of about 5). For constructing this model in the grid
102 domain, one must use 36936 unknown points, 25921 spherical cap harmonics coefficients (Al-
103 Fanek, 2013; Forootan et al., 2021), where the cap extension is required to solve the local
104 orthogonality.

105 To evaluate the performance of IR-ZWD, the outputs are compared with those of GPT3w
106 (Landskron and Böhm, 2018), GTrop (Sun et al., 2019), and HGPT2 (Mateus et al., 2021) models,
107 as well as the outputs of ERA5 during 1 January 2022 to 31 December 2022, which are not used

108 within the IR-ZWD model. Additionally, the outputs of IR-ZWD are compared with 5 located
109 radiosonde stations in Iran and the ZWD estimated from the Jason-3 satellite altimetry mission
110 (Dumont et al., 2016) over the Caspian Sea and the Persian Gulf.

111 In what follows, in section 2, the datasets and the study region are introduced. In Section 3, the
112 construction of the proposed empirical model is explained. In Section 4, the numerical results of
113 the study are presented, and finally in section 5, this study is concluded.

114

115 2. Data and region of study

116 2.1. Data

117 The European Centre for Medium-Range Weather Forecasts (ECMWF) has introduced the
118 Empirical Reanalysis Fifth Generation (ERA5) global meteorological model, which has a spatial
119 resolution of about 0.25 degrees and an hourly temporal resolution for 37 different pressure levels
120 ranging from 1 hPa to 1000 hPa (baba shaeb Kannemadugu et al., 2022; Forootan et al., 2021).
121 This dataset is freely accessible from <https://cds.climate.copernicus.eu/>. The numerical model
122 provides a wide range of meteorological parameters, including temperature, geopotential, and
123 relative humidity, which can be used to calculate wet refractivity indices at different pressure
124 levels. The geopotential data is employed to determine the corresponding ellipsoidal height of the
125 dataset (Ma et al., 2021). By incorporating the remaining meteorological parameters, the wet
126 refractivity indices can be calculated using :

$$e = \frac{RH \cdot \alpha_1 \cdot e^{\left(\frac{\alpha_2 \cdot t}{T + \alpha_3}\right)}}{100}, \quad (1)$$

$$N_w = 3.732 * 10^5 * \frac{e}{T^2}, \quad (2)$$

127 (Forootan et al., 2023), where e is the water vapor pressure in hPa, RH is relative humidity, t and
128 T are temperature in Celsius and Kelvin, respectively, and N_w is the wet refractivity index. The
129 constant coefficients of α_1 , α_2 , and α_3 are selected to be 6.1121, 17.502, and 240.97 respectively.
130 Using the wet refractivity indices of Eq. (?) at different altitudes, the Zenith Wet Delay (ZWD)
131 can be calculated by integrating them over the zenith direction as in (Bevis et al., 1992):

$$ZWD = 10^{-6} \int_L N_w dl . \quad (3)$$

132 The aim of this study was to develop a regional model for estimating ZWD values. To achieve this
133 goal, we used ERA5 data that include temperature, geopotential, and relative humidity from
134 January 1, 2017 to December 31, 2021. Since the wet refractivity indices tend to zero for altitudes
135 above 10 km, we selected only 16 levels (out of 37) from 1000 hPa to 250 hPa of ERA5 pressure
136 levels. Additionally, we used the data with a time resolution of approximately 6 hours (0, 6, 12,
137 and 18 UTC times) to establish the regional ZWD model. This is also justified because the finest
138 harmonics base functions used in the regional model has a period of three months (see section 4.1).
139 The study region is shown in Fig. 1 and contains 4104 unique grid points, for which we calculated
140 ZWD values using the 6-hourly inputs of 2017-2021.

141

Commented [EF3]: Check the reference!

142 2.2. The region of study

143 The study area has been selected to include Iran and the nearby regions, covering the latitudes
 144 between 25.5 to 39.5° and the longitudes 44.5 to 62.5°, with its altitudes ranging from
 145 approximately -37 to 2524 m (Fig. 1). This region is located in the mid-latitude zone and is
 146 influenced by its proximity to the Caspian Sea, the Persian Gulf, as well as Zagros, and Alborz
 147 Mountains, thus, resulting in diverse climates with local variations (Heydarizadeh Shali et al.,
 148 2020). Some regions experience arid and hot climates with low water vapor content, while others
 149 exhibit a more moderate climate with high water vapor content and rapid changes. To evaluate the
 150 proposed model's derived ZWD values, the study uses observations from 5 existing radiosonde
 151 stations and the valid microwave radiometer of Jason-3. Fig. 1 shows the location of the radiosonde
 152 stations and Jason-3 ZWD observations in the study area, and Table 2 lists the geographical
 153 coordinates of the radiosonde stations.

154

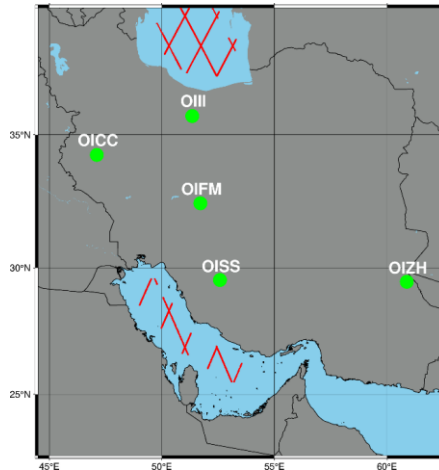


Fig. 1. The presentation of the region of study. The green dots show the location of 5 radiosonde stations (location are reported in Table 2) in the region. Also, the red dots display the Jason-3 ZWD observations (cycles 217-325), including the path numbers ?.

155

156 **Table 2.** Geographical coordinates of radiosonde stations.

Station name	Latitude(deg)	Longitude(deg)	Altitude(m)
OICC	34.26	47.11	1322
OIFM	32.46	51.71	1550
OIHH	35.68	51.35	1191
OISS	29.53	52.58	1491
OIZH	29.46	60.88	1370

157

158

159 3. Methodology

160 3.1. Quadratic B-spline Functions

161 The B-spline functions are often used for local and global signal localization due to their compact
 162 support (Nohutcu et al., 2010). These functions are commonly implemented in Euclidean space
 163 and can be used to decompose target parameters into a series of detailed signals via consecutive
 164 low-pass filters (Limberger, 2015). A one-dimensional signal can be expanded in terms of B-spline
 165 functions using:

$$g(x) = \sum_{h=0}^{h_s} \alpha_h^s \varphi_h^{m,s}(x), \quad (4)$$

166

167 (Schmidt et al., 2008), where $g(\cdot)$ is the considered signal, α_k^s are the coefficients of the base
 168 function, φ_k^s are the kernel of the normalized polynomial B-splines of order m , s is the surface
 169 resolution for corresponding kernel, and h_s is set of polynomial B-splines for selected surface
 170 resolution and is equal to:

$$171 \quad h_s = 2^s + m - 1. \quad (5)$$

172 The number of coefficients for retrieving $g(x)$ is also equal to h_s . The base function with order m
 173 and the corresponding surface resolution can be calculated in a recursive procedure as:

$$\varphi_h^{m,s}(x) = \frac{x - t_h^s}{t_{h+m}^s - t_h^s} \varphi_h^{m-1,s}(x) + \frac{t_{h+m+1}^s - x}{t_{h+m+1}^s - t_{h+1}^s} \varphi_{h+1}^{m-1,s}(x) \quad (6)$$

174

$$\varphi_h^{0,s}(x) = \begin{cases} 1 & t_h^s \leq x < t_{h+1}^s \\ 0 & \text{else} \end{cases}. \quad (7)$$

175 (Limberger, 2015). In these expressions, t_h^s are knots and the number of them are equals to $2^s +$
 176 2 and control the spatial resolution of B-spline functions (Schmidt et al., 2008). For the 2D
 177 modeling of a parameter, Eq. (1) can be expanded as:

$$g(x_1, x_2) = \sum_{h_1=0}^{h_{s_1}} \sum_{h_2=0}^{h_{s_2}} \alpha_{h_1, h_2}^{s_1, s_2} \varphi_{h_1}^{m, s_1}(x_1) \varphi_{h_2}^{m, s_2}(x_2). \quad (8)$$

178

179 In this case, the number of coefficients ($\alpha_{h_1, h_2}^{s_1, s_2}$) are about $h_{s_1} \times h_{s_2}$. In order to reconstruct the
 180 $g(x_1, x_2)$ function, the mentioned coefficients need to be estimated, where the computation
 181 procedure follows a least squares optimization, see section 3.2.

182

183 3.2. The IR-ZWD model

184 The values of ZWD exhibit a periodical change, which is usually modeled using sinusoidal and
 185 cosine functions (YAO et al., 2013; Yao et al., 2016). Based on the characteristics of ZWD values,
 186 the considered periodical model can be written as follows:

$$ZWD(\varphi, \lambda, h) = \left[a_0(\varphi, \lambda) + \sum_{i=1}^4 \left(a_i(\varphi, \lambda) \cos\left(\frac{i \cdot 2\pi \cdot doy}{365.25}\right) + b_i(\varphi, \lambda) \sin\left(\frac{i \cdot 2\pi \cdot doy}{365.25}\right) \right) \right] e^{-\vartheta h} \quad (9)$$

$$a_i(\varphi, \lambda) = \sum_{h_1=0}^{h_{s_1}} \sum_{h_2=0}^{h_{s_2}} \alpha_{h_1, h_2}^{s_1, s_2} \varphi_{h_1}^{m, s_1}(\varphi) \varphi_{h_2}^{m, s_2}(\lambda). \quad (10)$$

187
 188 where φ and λ are the geographical latitude and longitude, h is the height, doy is the day of the
 189 year, ϑ is the height scale, and is about -0.00013137 (Yao et al., 2016). The considered periodical
 190 variation of ZWD values are the mean value (a_0), annual variations (a_1 and b_1), semi-annual
 191 variations (a_2 and b_2), 4-monthly variations (a_3 and b_3), and 3-monthly variations (a_4 and b_4). In
 192 this model, the coefficients a_i & b_i , $i = 1, 2, 3, 4$, are determined using B-spline functions.
 193 Therefore, for implementing the IR_ZWD models, the B-spline coefficients ($\alpha_{h_1, h_2}^{s_1, s_2}$) for each
 194 amplitude must be determined. Here the ZWD values are computed using the ERA5 data of 2017-
 195 2021. The corresponding B-spline coefficients are computed using the least squares method (Koch,
 196 2007). After the estimation of B-spline coefficients, the amplitude (Amp , except for the mean value
 197 (a_0)) can be calculated as:

$$Amp(\varphi, \lambda) = \sqrt{a_i(\varphi, \lambda)^2 + b_i(\varphi, \lambda)^2}. \quad (11)$$

198 To build the B-spline expansion of the ZWD fields, one needs to select the order and resolution of
 199 B-splines. The higher number of parameters, results in a higher resolution. However, considering
 200 too high number for these parameters results in huge number of model coefficients which are not
 201 desired (reference?). Therefore, the accuracy of the results is correlated with these parameters and
 202 needs to be examined. Our numerical experiment is described in section 4.1.

203 For examining the accuracy and reliability of the proposed model, the Root Mean Squared Error
 204 (RMSE), the squared Correlation Coefficients (CC), and the Mean Absolute Error (MAE) are
 205 calculated as:

$$MAE = \frac{1}{n} \sum_{i=1}^n ZWD_m^i - ZWD_o^i. \quad (12)$$

$$RMSE = \sqrt{\frac{\sum_{i=1}^n (ZWD_m^i - ZWD_o^i)^2}{n}}. \quad (13)$$

$$CC = 1 - \left(\frac{\sum_{i=1}^n (ZWD_m^i - ZWD_o^i)^2}{\sum_{i=1}^n (ZWD_o^i - \overline{ZWD_o})^2} \right). \quad (14)$$

206 In the mentioned expressions, ZWD_m and ZWD_o correspond to the modeled and observed values,
 207 respectively, and $\overline{ZWD_o}$ represents the mean observed value.

208

209 4. Results

210

211 4.1. Determination of the B-spline parameters

212 The spatial resolution of the functional models depends on the properties of their base functions,
 213 which is in this case, consists of the defined B-spline parameters in Eq. (10). Besides, the temporal
 214 resolution of the model is controlled by the number and frequency of the (temporal) harmonics in
 215 Eq. (9). Therefore, for constructing the IR-ZWD model, the order of temporal resolution (i in Eq.
 216 (9)), the surface resolution of B-splines (s), and the order of B-splines (m) in Eq. (10) needs to be
 217 fixed. These parameters have been determined empirically by developing the IR-ZWD model for
 218 the considered groups of parameters. For this, in an empirical approach, the model has been
 219 developed for different groups of parameters and the corresponding performance has been
 220 examined (Al-Fanek, 2013; Forootan et al., 2021; Razin and Voosoghi, 2017). For implementing
 221 the B-spline, the order and surface resolutions are considered to be between 2 and 3 and 2 to 5,
 222 respectively. The temporal resolution is selected to be up to semi-annual variations ($i = 1$ and 2),
 223 up to 4-month variations ($i = 1, 2, 3$), and up to 3-month variations ($i = 1, 2, 3, 4$). For
 224 each case, a set of model parameters (e.g. B-spline order, B-spline surface resolution, and temporal
 225 resolution) has been used for developing the proposed model using 20% of the ERA5 data from
 226 years 2017-2021 that have been randomly used. Afterwards, ZWD values are computed using the
 227 developed model, for each case, and the RMSE value (Eq. (13)) was calculated with respect to the
 228 original ERA5 values. Accordingly, the group of parameters that provided the minimum mean
 229 RMSE is selected as the “optimal” functional model parameters. Table 3 reports the results of this
 230 comparison, where the 3 last columns list the RMSE values for different temporal resolutions of
 231 the proposed model.

232

233

Table 3. RMSE values for various group of functional model parameters.

B-spline order(m)	B-spline resolution(s)	Semi-annual (i=2)	4-monthly (i=3)	3-monthly (i=4)
		RMSE(m)	RMSE(m)	RMSE(m)
2	2	0.040	0.0393	0.0382
2	3	0.0388	0.0380	0.0369
2	4	0.0380	0.0372	0.0361
2	5	0.0374	0.0367	0.0355
3	2	0.0395	0.0388	0.0376
3	3	0.0386	0.0379	0.0367
3	4	0.0379	0.0371	0.0360

3	5	0.0374	0.0367	0.0355
---	---	--------	--------	--------

234

235 Given the RMSE values in Table 1, it can be concluded that by increasing the number of model
 236 parameters, the RMSE value drops, and the minimum RMSE derived by considering model
 237 parameters as $m = 3, s = 5, i = 4$. As mentioned, the motivation for using the B-spline function
 238 as the functional model was to decrease the model parameters compared to the grid-based
 239 approach. Considering the grid-based formulation with a temporal resolution up to 3-months
 240 results in 9 model parameters for each point, and overall 36936 parameters for this model.
 241 However, our proposed model, that contains B-spline functions, contains 10404 parameters, which
 242 are less than the grid-based approach making the computation more stable. The region of study
 243 covers about $18^\circ \times 14^\circ$ in longitude and latitude directions. According to the considered surface
 244 resolution of the B-spline, the number of knots is about 32. Therefore, the spatial resolution of the
 245 considered B-spline functions is $\sim 0.5^\circ$. As a result, given the geographical coordinates and the day
 246 of the year, using the IR-ZWD model, the ZWD value can be calculated for the entire study region.

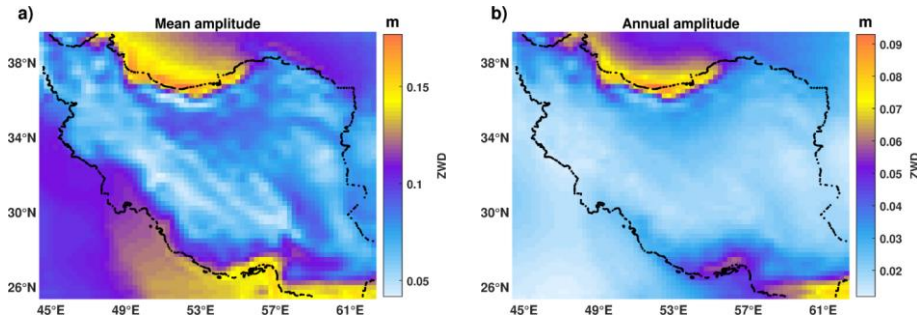
247

248 4.2. The amplitude of temporal variations

249 The regional ZWD model was constructed using ERA5 data from 2017 to 2021, and the
 250 corresponding B-spline model with $m = 3, s = 5, i = 4$ as model parameters. Using Eq. (11), the
 251 amplitude of each considered periodic variation for the corresponding regional model can be
 252 calculated. Fig. 2 displays the amplitudes of the mean, annual, semi-annual, 4-month, and 3-month
 253 variations over the study area.

254

Commented [EF4]: Table 3?



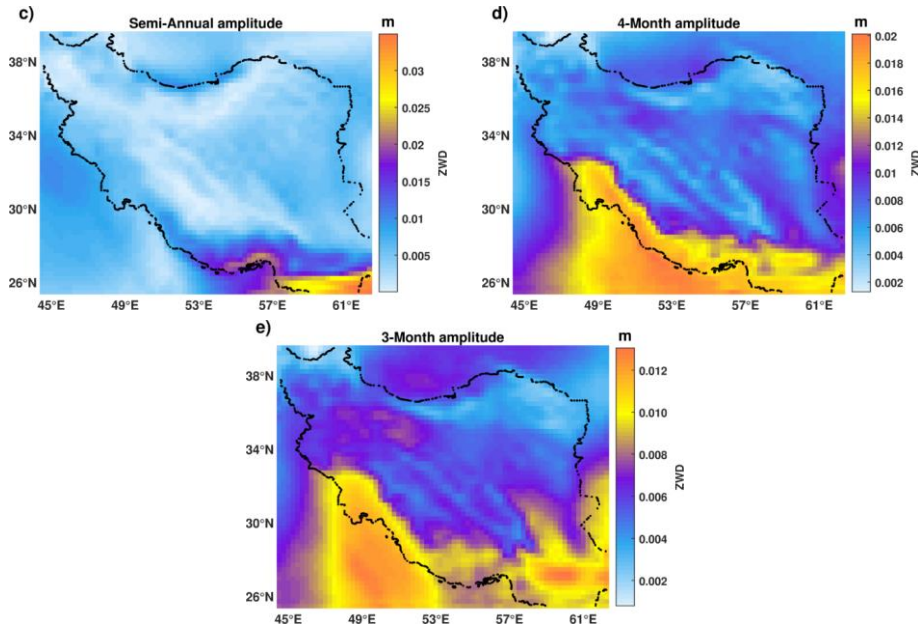


Fig. 2. An overview of the amplitude of the mean (a), annual (b), semi-annual (c), 4-monthly (d), and 3-monthly (e) variations of IR-ZWD over the considered region.

255 From Fig. 2, it can be observed that the reduction of the period of variations is accompanied by a
 256 decrease in the amplitude of the corresponding component. As depicted in Fig. 2, the maximum
 257 mean amplitude of ZWD corresponds to the regions over or near the oceans in the study area,
 258 which is expected due to the higher amount of water vapor in these regions. Similarly, the
 259 maximum amplitude of the annual variations also corresponds to these regions due to the high
 260 contribution of water vapor content. Moreover, the strongest semi-annual amplitude is observed
 261 in the southeast regions, reaching up to 3 centimeters, and can be related to the monsoon effect
 262 (Vuille et al., 2005). We found the near ocean region such as those in the southern part of the study
 263 area to be associated with the maximum amplitude of the 4- and 3-monthly variations, which reach
 264 up to 2 and 1 cm, respectively. This is due to seasonal changes in the ZWD values which show a
 265 higher amplitude in coastal areas.

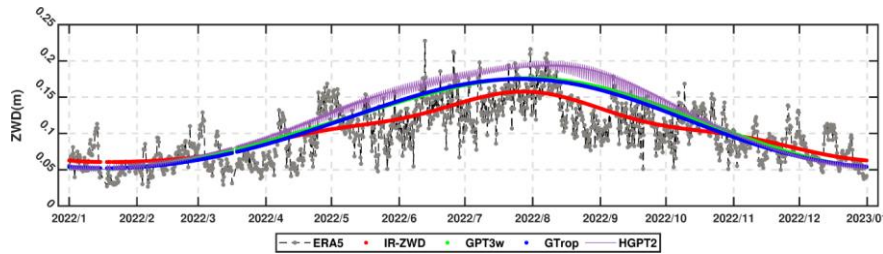
266 Using the estimated B-spline coefficients, geographical longitude and latitude, and the day of the
 267 year (DOY), ZWD can be calculated using the proposed regional model. In the following, the
 268 constructed model has been evaluated using ERA5 ZWD data for the entire year 2022. For this
 269 case, the ZWD values derived from the proposed model, as well as those calculated from the
 270 GPT3w, GTrop, and HGPT2 models, will be compared with the corresponding ERA5 values.
 271 Afterwards, to evaluate the proposed model using a different dataset, the obtained ZWD values
 272 from the IR_ZWD model will be compared with the corresponding values from six radiosonde
 273 stations and Jason-3 radiometer measurements in the study region.

274

275 4.3. Comparison with the ERA5 ZWD values

276 In this section, the performance of models is compared to the ERA5 ZWD values for the time
277 period of January 1, 2022 to December 31, 2022. For this, we calculated ZWD values from IR-
278 ZWD, GPT3w, GTrop, and HGPT2 at the same grid points as the ERA5 dataset and with a time
279 resolution of approximately 6 hours (0, 6, 12, and 18 UTC times). The calculated ZWD time series
280 from these models are then compared with the corresponding ERA5 values at each grid point, and
281 the statistical values are computed for each grid point. For example, Fig. 3 shows the comparison
282 for a grid point with the latitude=39°, the longitude=45.75°, and the altitude=833m. This location
283 is selected because that of IRI-ZWD was different from other models.

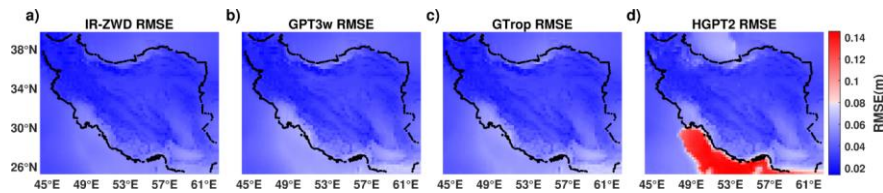
284



285 Fig. 3. The ZWD values of a grid point with latitude=39°, longitude=45.75°, and altitude=833m from ERA5 data, IR-ZWD, GPT3w, GTrop, and HGPT2 models with gray, red, green, blue, and purple lines, respectively.

286 In Fig. 3, the RMSE of the IR-ZWD, GPT3w, GTrop, and HGPT2 models are found to be about
287 0.025, 0.032, 0.031, and 0.039 m, respectively. This shows IR-ZWD provides a slightly better
288 regional fit to ERA5. Fig. 4 displays the calculated statistical values for each model at each grid
289 point across the study region. Additionally, Fig. 5 depicts the Taylor diagram for the mean RMSE
290 and CC values obtained from the evaluation of these models.

291



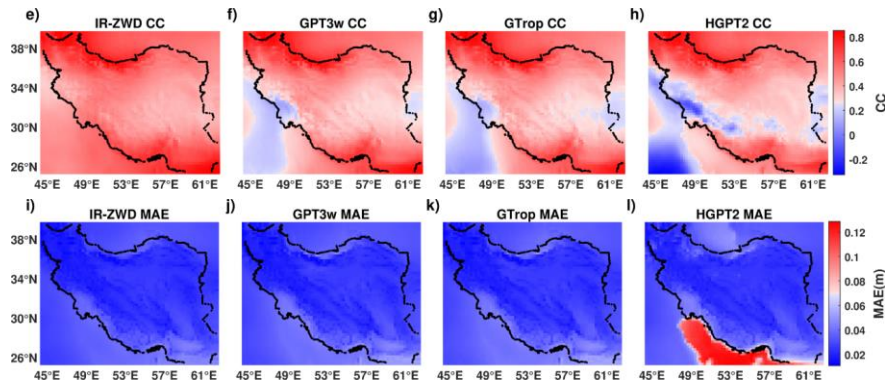


Fig. 4. An overview of the RMSE values for the IR-ZWD, GPT3w, GTrop, and HGPT2 models over the study region, which are in the subplot a, b, c, and, d, respectively. Figures e, f, g, and h show the corresponding CC values of the considered models. Also, the distribution of the calculated MAE values for considered models has been depicted in i, j, k, and l figures. These parameters are calculated through comparison with the ERA5 ZWD values from 1 January 2020–31 December 2022.

292

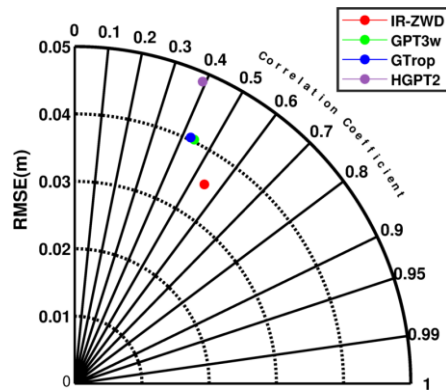


Fig. 5. An overview of the calculated mean RMSE and CC values over the region of study based on the Taylor diagram.

293

294 Considering Fig. 4a, b, c, and d, we found that the RMSE values of the IR-ZWD model to be lower
 295 than the corresponding values of GPT3w ,GTrop, and HGPT2 models in regions over or nearby
 296 oceans or seas. These areas have the highest water vapor content and its variations. Therefore,
 297 developing the IR-ZWD model with a higher spatial and temporal resolution has improved the
 298 accuracy in these regions. Additionally, Fig. 5 shows that the mean RMSE of IR-ZWD is about
 299 0.035 m, indicating an improvement of approximately 12.5% compared to the GPT3w and GTrop
 300 models, and improvement of about 27.5% compared to HGPT2 model. Comparing the CC values
 301 in Fig. 4e, f, g, and h, it can be seen that the proposed model greatly improved the CC values in

302 regions where the corresponding values of GPT3w, GTrop, and HGPT2 were low (the region with
 303 the blue colors in Fig. 4f, g, and h). Moreover, as illustrated in Fig. 5, the mean CC of IR-ZWD,
 304 i.e., about 0.55, is approximately 10, 11, and 15% higher than the corresponding CC values of
 305 GPT3w, GTrop, and HGPT2. The mean MAE values for IR-ZWD, GPT3w, GTrop, and HGPT2
 306 models are found to be about 0.028, 0.030, 0.030, and 0.037 m, respectively. These values indicate
 307 an improvement of approximately 7, 7, and 29% in the MAE value of IR-ZWD compared to the
 308 GPT3w, GTrop, and HGPT2 models. By comparing the statistical parameters in Fig. 5, it can be
 309 seen that GPT3w slightly outperforms the GTrop model over the study region. It should be noted
 310 that the spatial resolution of the two models is the same and GTrop is constructed with a higher
 311 temporal resolution. Referring Fig. 4d and l, it becomes evident that, for the southern part of the
 312 study region (including the Persian Gulf and the Oman Sea), the RMSE and MAE values of the
 313 HGPT2 model are higher than those of other models.

314 To compare the performance of IR-ZWD at different altitudes, we examined the mean RMSE
 315 calculated at each grid point of ERA5 data (Fig. 4a, b, c, and d) and considered the corresponding
 316 altitudes of the points. Fig. 6 shows the mean RMSE of each ERA5 grid point for the IR-ZWD,
 317 GPT3w, GTrop, and HGPT2 models, plotted against the altitude of each point. The vertical profile
 318 of the mean RMSE for each model is also shown in this figure.

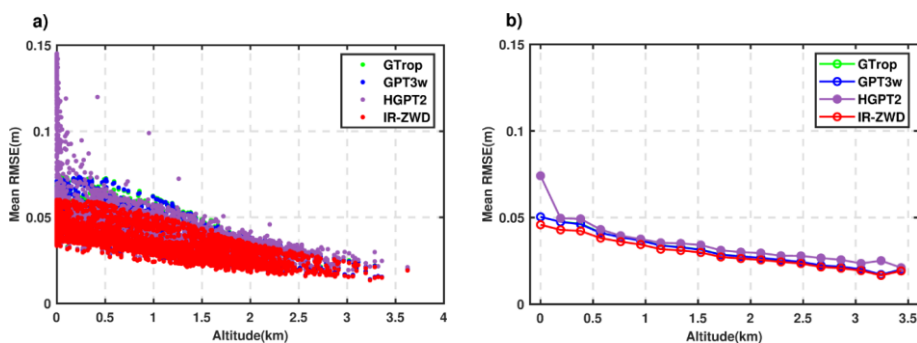


Fig. 6. An overview of a) the comparison of the mean RMSE values for different grid points with respect to the altitude of each point. the mean RMSE of GTrop, GPT3w, HGPT2, and IR-ZWD models are displayed with green, blue, purple, and red lines respectively. In b) the vertical profile of the mean RMSE value for each model is provided.

319 From Fig. 6, it can be seen that the performance of the IR-ZWD model for all altitudes is relatively
 320 closer to observations compared to other models. Fig. 6b compares the mean RMSE of three
 321 models for points with a low altitude (between 0 and 1 km), which that of IR-ZWD is 0.045 m
 322 compared with 0.05, 0.05, and 0.074 m from GPT3w, GTrop, and HGPT2 models. while the
 323 performance of all three models is found almost similar for points with high altitudes. According
 324 to the RMSE values depicted in Fig. 6a, for the HGPT2 model, one can infer that the model's
 325 accuracy is comparatively lower for points with low altitudes compared to the GPT3w and GTrop
 326 models.

327

328 4.4. Comparison with the radiosonde measurements

329 A radiosonde is an instrument attached to a balloon that rises up to different atmospheric layers
330 and measures several atmospheric parameters that can be used to calculate wet refractivity indices
331 and thus ZWD values. These measurements are provided twice per day (at 12 and 24 UTC time)
332 and, due to their high accuracy, are always considered as a reference for evaluation in atmospheric-
333 related research (Adavi and Mashhadi-Hossainali, 2014; Bender et al., 2011; Forootan et al., 2023;
334 Forootan et al., 2021). In this section, to further evaluate the estimated ZWD values from models,
335 they are compared with the data from five existing radiosonde stations in the study region (Fig. 1).
336 This evaluation is done over the period of January 1, 2022 to December 31, 2022, where data were
337 not used in the modelling but were available for validation. The radiosonde data have been
338 obtained from <http://weather.uwyo.edu/upperair/sounding.html>. Fig. 7 shows the results of IR-
339 ZWD, GPT3w, GTrop, and HGPT2 ZWD. The calculated statistical parameters are depicted in
340 Fig. 8.

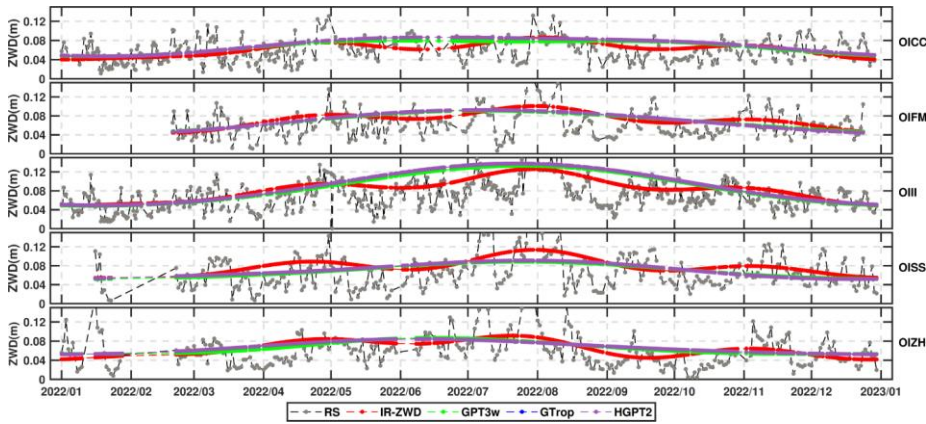


Fig. 7. An overview of the validation of ZWD estimated from the four considered models with corresponding measurements of 5 existing radiosonde stations in the study region. The gray, red, green, blue, and purple dots correspond to the radiosonde, IR-ZWD, GPT3w, GTrop, and HGPT2 ZWD values, respectively.

341

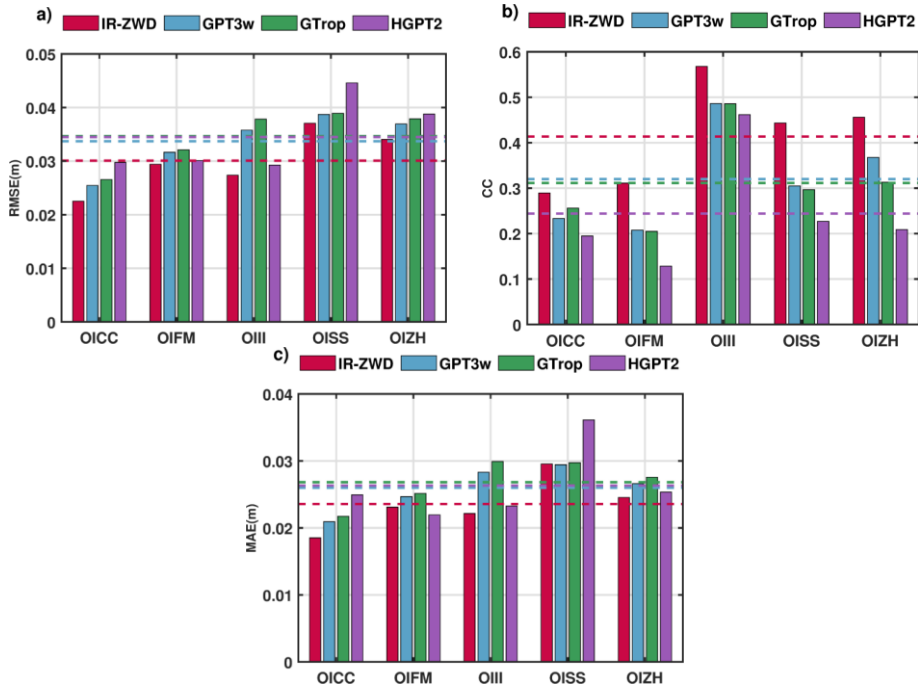


Fig. 8. A summary of the calculated RMSE, CC, and MAE statistic parameters for each radiosonde station in a, b, and c, respectively. The bars with the red, cyan, green, and purple colors are for the IR-ZWD, GPT3w, GTrop, and HGPT2 models, respectively. Also, the mean value of each parameter has been shown with the corresponding dashed lines.

342 Fig. 8a shows that the mean RMSE of IR-ZWD model is about 0.03 m, indicating an improvement
 343 of about 11%, 13%, and 13% compared to GPT3w, GTrop, and HGPT2, respectively. In Fig. 8b,
 344 the mean CC value of IR-ZWD is found to be about 0.41, which is approximately 10, 10, and 17%
 345 higher than the corresponding values for the GPT3w, GTrop, and HGPT2 models, respectively.
 346 Additionally, Fig. 8c displays the IR-ZWD mean MAE value of 0.023 m, indicating an
 347 improvement of about 9, 12, and 12% compared to the GPT3w, GTrop, and HGPT2 models,
 348 respectively. These statistical measures are found to be consistent with those reported in the
 349 comparison with ERA5 data except for statistic parameters from the HGPT2 model. It is worth
 350 noting that the higher improvement in RMSE for IR-ZWD is observed at the OIII station, as shown
 351 in Fig. 8a. Referring to Table 2, we can see that this station has the lowest altitude among the
 352 considered radiosonde stations. Thus, consistent with the results of the comparison with ERA5
 353 data, the IR-ZWD model outperforms the GPT3w and GTrop models for locations of lower
 354 altitudes with higher vapor fluctuations. Comparing RMSE values of the HGPT2 model in Fig. 8
 355 and Fig. 5, it can be seen that the RMSE value of the HGPT2 model is lower when compared to
 356 radiosonde stations (about 28% lower). Referring to Fig. 4d, it can be seen that the RMSE values
 357 of the HGPT model for land areas are almost the same as the GPT3w and GTrop models. Thus,
 358 considering the fact that the considered radiosonde stations are located inland areas, it can be

359 concluded that the performance of the HGPT2 model only in the Persian Gulf and Oman Sea is
360 weaker than the GPT3w and GTrop models.

361

362 4.5. Comparison with the Jason-3 radiometer measurements

363 One of the valuable sources of water vapor-related observations over oceans is measurements from
364 equipped radiometers in altimetry missions. The Jason-3 mission was launched in 2016 with the
365 Advanced Microwave Radiometer-2 (AMR-2) to correct the effect of ZWD value in satellite range
366 observations (Gong and Liu, 2020). The presence of the Caspian Sea and Persian Gulf in the study
367 region provides an opportunity to further evaluate the IR_ZWD model with respect to estimated
368 ZWD values from Jason-3 radiometer observations. For this purpose, IR-ZWD model was
369 compared with the Jason-3 ZWD values over the time interval of 1 January 2022 to 31 December
370 2022 (Jason-3 cycles 217-325). The Jason-3 data can be downloaded from
371 <https://www.aviso.altimetry.fr>. Radiometer observations are unreliable and biased near coastal
372 regions (Desportes et al., 2007). Therefore, only observations with a distance of more than 50 km
373 from the nearest coastal region were considered (the points with valid ZWD observations have
374 been displayed in Fig. 1). Hence, the valid Jason-3 radiometer measurements were about 6251 in
375 the study region. Fig. 9 shows the joint Kernel Density Estimate plots of IR-ZWD, GPT3w, GTrop,
376 and HGPT models in comparison with the Jason-3 estimated ZWD value that have been plotted
377 using the Seaborn library in the Python (Waskom et al., 2014). These plots show the comparison
378 of the modeled ZWD values versus the objective one and the contributed blue colored points,
379 indicate the probability of each value. The corresponding Taylor diagram for calculated statistical
380 parameters has been displayed in Fig. 10.

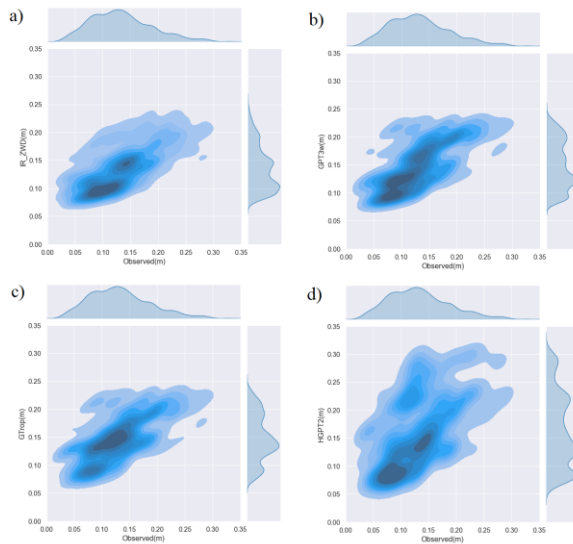


Fig. 9. An overview of the joint Kernel Density Estimate (KDE) plots of Jason-3 ZWD values versus the IR-ZWD (a), GPT3w (b), GTrop (c), and HGPT (d) models, respectively.

381

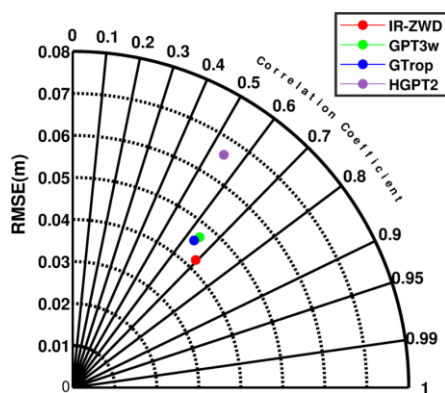


Fig. 10. An overview of the Taylor Diagram for comparing the ZWD estimated from Jason-3 with those of IR-ZWD, GPT3w, GTrop, and HGPT2. Radial and angular directions stand for different RMSE and CC values. The red, green, blue, and purple dots represent the IR-ZWD, GPT3w, GTrop, and HGPT2 models, respectively.

382

383 According to Fig. 10, the RMSE of IR-ZWD model is about 0.042 m, which indicates an
 384 improvement of approximately 10%, 7%, and 36% compared to the GPT3w, GTrop, and HGPT2
 385 models, respectively. The CC of IR-ZWD model is found to be approximately 0.69, which is about
 386 5%, 6%, and 15% higher than the corresponding CC values for GPT3w, GTrop, and HGPT2
 387 models, respectively. Additionally, the calculated MAE value for IR-ZWD is found to be 0.031
 388 m, which represents improvements of approximately 11%, 7%, and 36% compared to GPT3w,
 389 GTrop, and HGPT2 models, respectively. Referring to Fig. 10, in comparison with Jason-3
 390 radiometer measurements, the HGPT2 model exhibits an RMSE of approximately 0.066 m,
 391 signifying the weakest performance among the considered models in the Persian Gulf and Oman
 392 Sea regions.

393

394 5. Conclusion

395 Atmospheric delay, specifically the Zenith Wet Delay (ZWD), is a challenging parameter to
 396 empirically parameterize due to high spatiotemporal variations. As it is the main source of error in
 397 space-based geodetic observations, constructing a reliable empirical model for real-time
 398 applications in positioning and weather prediction is crucial. However, in data sparse regions like
 399 Iran that exhibits considerable spatial and temporal vapor variations, the application of global
 400 atmospheric models might represent limited skills for positioning applications. In this study, we
 401 developed a regional ZWD model for a region including Iran, thus called the IR-ZWD model,
 402 which uses local base functions for an effective representation of the spatial distribution. This
 403 model incorporates ERA5 data from 2017-2022 to construct the model over five different time

404 scales: mean, annual, semi-annual, 4-monthly, and 3-monthly variations. We optimized the
405 structure of the model empirically and compared its result with the ZWD values from ERA5 data
406 over the time interval outside of the fitting period (i.e., January 1, 2022, to December 31, 2022),
407 and found that IR-ZWD has the least mean RMSE of about 0.035 m over the region of study. This
408 is about 12.5% better than the global GPT3w and GTrop models, and 27.5% better than the HGPT2
409 model. Additionally, the squared correlation coefficient of IR-ZWD is found to be 0.55, i.e., about
410 10% higher than the other models. To further evaluate the accuracy of our proposed model, we
411 compared the ZWD values from IR-ZWD with five located radiosonde stations in the region of
412 study. We found that the mean RMSE of IR-ZWD is about 0.03 m, 11%, 13%, and 13% lower
413 than the GPT3w, GTrop, and HGPT2 models, respectively. Furthermore, the derived CC value of
414 the IR_ZWD model was about 0.41, which was about 10% higher than the corresponding GPT3w
415 and GTrop models, and 17% higher than the CC value from the HGPT2 model. Finally, we
416 compared the ZWD values from our model with corresponding Jason-3 radiometer measurements.
417 The IR-ZWD model showed an improvement of about 10%, 6%, and 11% in RMSE, CC, and
418 MAE values, respectively, compared to the GPT3w and GTrop models. Overall, our results
419 suggest that the IR-ZWD model has higher accuracy than global empirical models and that our
420 proposed method increases the reliability of the estimated ZWD values. In future, the impact of
421 IR-ZWD for Standard Point Positioning (SPP) applications will be evaluated.

422

423 6. References

- 424 Adavi, Z., Mashhadi-Hossainali, M., 2014. 4D tomographic reconstruction of the tropospheric wet
425 refractivity using the concept of virtual reference station, case study: northwest of Iran. *Meteorology
426 and Atmospheric Physics* 126, 193-205.
- 427 Al-Fanek, O.J.S., 2013. Ionospheric imaging for Canadian polar regions. University of Calgary.
- 428 baba shaeb Kannemadugu, H., Ranganathan, K., Gharai, B., et al., 2022. GNSS-GPS derived integrated
429 water vapor and performance assessment of ERA-5 data over India. *Journal of Atmospheric and Solar-
430 Terrestrial Physics* 227, 105807.
- 431 Bender, M., Dick, G., Ge, M., et al., 2011. Development of a GNSS water vapour tomography system
432 using algebraic reconstruction techniques. *Advances in Space Research* 47, 1704-20.
- 433 Bevis, M., Businger, S., Herring, T.A., et al., 1992. GPS meteorology: Remote sensing of atmospheric
434 water vapor using the Global Positioning System. *Journal of Geophysical Research: Atmospheres* 97,
435 15787-801.
- 436 Black, H.D., 1978. An easily implemented algorithm for the tropospheric range correction. *Journal of
437 Geophysical Research: Solid Earth* 83, 1825-8.
- 438 Böhm, J., Möller, G., Schindelegger, M., et al., 2015. Development of an improved empirical model for
439 slant delays in the troposphere (GPT2w). *GPS solutions* 19, 433-41.
- 440 Collins, J.P., Langley, R.B. A tropospheric delay model for the user of the wide area augmentation
441 system. Department of Geodesy and Geomatics Engineering, University of New Brunswick ..., 1997.
- 442 Davis, J., Herring, T., Shapiro, I., et al., 1985. Geodesy by radio interferometry: Effects of atmospheric
443 modeling errors on estimates of baseline length. *Radio science* 20, 1593-607.
- 444 Dee, D.P., Uppala, S.M., Simmons, A.J., et al., 2011. The ERA-Interim reanalysis: Configuration and
445 performance of the data assimilation system. *Quarterly Journal of the royal meteorological society* 137,
446 553-97.

447 Dehvari, M., Karimi, S., Farzaneh, S., et al., 2023. Improving IRI-2016 Global Total Electron Content Maps
448 Using ELM Neural Network. *Advances in Space Research*.

449 Desportes, C., Obligis, E., Eymard, L., 2007. On the wet tropospheric correction for altimetry in coastal
450 regions. *IEEE transactions on geoscience and remote sensing* 45, 2139-49.

451 Dogan, A.H., Erdogan, B., 2022. A new empirical troposphere model using ERA5's monthly averaged
452 hourly dataset. *Journal of Atmospheric and Solar-Terrestrial Physics* 232, 105865.

453 Du, Z., Zhao, Q., Yao, W., et al., 2020. Improved GPT2w (IGPT2w) model for site specific zenith
454 tropospheric delay estimation in China. *Journal of Atmospheric and Solar-Terrestrial Physics* 198,
455 105202.

456 Dumont, J., Rosmorduc, V., Carrere, L., et al., 2016. Jason-3 products handbook. Technical
457 representative, CNES and EUMETSAT and JPL and NOAA/NESDIS.

458 Forootan, E., Dehvari, M., Farzaneh, S., et al., 2023. Improving the Wet Refractivity Estimation Using the
459 Extremely Learning Machine (ELM) Technique. *Atmosphere* 14, 112.

460 Forootan, E., Dehvari, M., Farzaneh, S., et al., 2021. A functional modelling approach for reconstructing 3
461 and 4 dimensional wet refractivity fields in the lower atmosphere using GNSS measurements. *Advances
462 in Space Research* 68, 4024-38.

463 Gong, Y., Liu, Z., 2020. Evaluating the accuracy of Jason-3 water vapor product using PWV data from
464 global radiosonde and GNSS stations. *IEEE Transactions on Geoscience and Remote Sensing* 59, 4008-17.

465 Hersbach, H., Bell, B., Berrisford, P., et al., 2020. The ERA5 global reanalysis. *Quarterly Journal of the
466 Royal Meteorological Society* 146, 1999-2049.

467 Heydarizadeh Shali, H., Sampietro, D., Safari, A., et al., 2020. Fast collocation for Moho estimation from
468 GOCE gravity data: the Iran case study. *Geophysical Journal International* 221, 651-64.

469 Hopfield, H., 1969. Two-quartic tropospheric refractivity profile for correcting satellite data. *Journal of
470 Geophysical research* 74, 4487-99.

471 Kalita, J., Rzepecka, Z., 2017. Impact of the initial tropospheric zenith path delay on precise point
472 positioning convergence during active conditions. *Measurement Science and Technology* 28, 045102.

473 Landskron, D., Böhm, J., 2018. VMF3/GPT3: refined discrete and empirical troposphere mapping
474 functions. *Journal of Geodesy* 92, 349-60.

475 Li, W., Yuan, Y., Ou, J., et al., 2012. A new global zenith tropospheric delay model IGGtrop for GNSS
476 applications. *Chinese science bulletin* 57, 2132-9.

477 Limberger, M., 2015. Ionosphere modeling from GPS radio occultations and complementary data based
478 on B-splines. *Technische Universität München*.

479 Ma, Y., Liu, H., Xu, G., et al., 2021. Empirical orthogonal function analysis and modeling of global
480 tropospheric delay spherical harmonic coefficients. *Remote Sensing* 13, 4385.

481 Ma, Y., Liu, T., Chen, P., et al., 2022. Global tropospheric delay grid modeling based on Anti-Leakage
482 Least-Squares Spectral Analysis and its validation. *Journal of Atmospheric and Solar-Terrestrial Physics*
483 229, 105829.

484 Mateus, P., Catalão, J., Mendes, V.B., et al., 2020. An ERA5-based hourly global pressure and
485 temperature (HGPT) model. *Remote Sensing* 12, 1098.

486 Mateus, P., Mendes, V.B., Plecha, S.M., 2021. HGPT2: An ERA5-based global model to estimate relative
487 humidity. *Remote Sensing* 13, 2179.

488 Nohutcu, M., Karslioglu, M., Schmidt, M., 2010. B-spline modeling of VTEC over Turkey using GPS
489 observations. *Journal of Atmospheric and Solar-Terrestrial Physics* 72, 617-24.

490 Penna, N., Dodson, A., Chen, W., 2001. Assessment of EGNOS tropospheric correction model. *The
491 Journal of Navigation* 54, 37-55.

492 Plag, H.-P., Rothacher, M., Pearlman, M., et al., 2009. The global geodetic observing system. *Advances in
493 Geosciences: Volume 13: Solid Earth (SE)*. World Scientific, 105-27.

494 Razin, M.R.G., Voosoghi, B., 2017. Regional ionosphere modeling using spherical cap harmonics and
495 empirical orthogonal functions over Iran. *Acta Geodaetica et Geophysica* 52, 19-33.

496 Saastamoinen, J., 1972. Atmospheric correction for the troposphere and stratosphere in radio ranging
497 satellites. *The use of artificial satellites for geodesy* 15, 247-51.

498 Schmidt, M., Bilitza, D., Shum, C., et al., 2008. Regional 4-D modeling of the ionospheric electron density.
499 *Advances in Space Research* 42, 782-90.

500 Subirana, J.S., Hernandez-Pajares, M., Zornoza, J.e.M.J. *GNSS Data Processing: Fundamentals and*
501 *Algorithms*. European space agency, 2013.

502 Sun, J., Wu, Z., Yin, Z., et al., 2017a. A simplified GNSS tropospheric delay model based on the nonlinear
503 hypothesis. *GPS Solutions* 21, 1735-45.

504 Sun, L., Chen, P., Wei, E., et al., 2017b. Global model of zenith tropospheric delay proposed based on
505 EOF analysis. *Advances in Space Research* 60, 187-98.

506 Sun, Z., Zhang, B., Yao, Y., 2019. A global model for estimating tropospheric delay and weighted mean
507 temperature developed with atmospheric reanalysis data from 1979 to 2017. *Remote Sensing* 11, 1893.

508 Tregoning, P., Herring, T.A., 2006. Impact of a priori zenith hydrostatic delay errors on GPS estimates of
509 station heights and zenith total delays. *Geophysical Research Letters* 33.

510 Tunalı, E., Özlüdemir, M.T., 2019. GNSS PPP with different troposphere models during severe weather
511 conditions. *GPS Solutions* 23, 82.

512 Vedel, H., Huang, X.-Y., 2004. Impact of ground based GPS data on numerical weather prediction.
513 *Journal of the Meteorological Society of Japan*. Ser. II 82, 459-72.

514 Vuille, M., Werner, M., Bradley, R., et al., 2005. Stable isotopes in precipitation in the Asian monsoon
515 region. *Journal of Geophysical Research: Atmospheres* 110.

516 Waskom, M., Botvinnik, O., Hobson, P., et al., 2014. *Seaborn: V0. 5.0* (November 2014). Zenodo.

517 Yan, X., Ducrocq, V., Poli, P., et al., 2009. Impact of GPS zenith delay assimilation on convective-scale
518 prediction of Mediterranean heavy rainfall. *Journal of Geophysical Research: Atmospheres* 114.

519 YAO, Y.-B., HE, C.-Y., Zhang, B., et al., 2013. A new global zenith tropospheric delay model GZTD. *Chinese*
520 *Journal of Geophysics* 56, 2218-27.

521 Yao, Y., Hu, Y., 2018. An empirical zenith wet delay correction model using piecewise height functions.
522 *Annales Geophysicae*. Copernicus GmbH, pp. 1507-19.

523 Yao, Y., Hu, Y., Yu, C., et al., 2016. An improved global zenith tropospheric delay model GZTD2
524 considering diurnal variations. *Nonlinear processes in geophysics* 23, 127-36.

525